Accurate simulation of two-dimensional optical microcavities with uniquely solvable boundary integral equations and trigonometric Galerkin discretization

Svetlana V. Boriskina, Phillip Sewell, and Trevor M. Benson

George Green Institute for Electromagnetics Research, University of Nottingham, University Park, Nottingham NG7 2RD, UK

Alexander I. Nosich

Institute of Radio Physics and Electronics, National Academy of Sciences of Ukraine, ul. Proskury 12, Kharkov 61085, Ukraine

A fast and accurate method is developed to compute the natural frequencies and scattering characteristics of arbitrary-shape two-dimensional dielectric resonators. The problem is formulated in terms of a uniquely solvable set of second-kind boundary integral equations and discretized by the Galerkin method with angular exponents as global test and trial functions. The log-singular term is extracted from one of the kernels, and closed-form expressions are derived for the main parts of all the integral operators. The resulting discrete scheme has a very high convergence rate. The method is used in the simulation of several optical microcavities for modern dense wavelength-division-multiplexed systems. © 2004 Optical Society of America

OCIS codes: 230.5750, 140.4780, 290.0290, 260.2110, 000.3860.

1. INTRODUCTION

Dielectric and semiconductor optical microcavities of various shapes have become popular wavelength-selective optical components for filtering, switching, lasing, modulation, and spectroscopy.[1–12] One of the attractive features of such microcavities is that they can support several types of natural eigenmodes that have significantly different Q factors and radiation characteristics. They are therefore suitable for different filter and laser applications. The fabrication of large (10–100-μm-sized) optical cavities based on the waveguide structures with low refractive-index contrast has long been achieved with standard photolithography techniques. These large low-confinement cavities can be simulated with acceptable accuracy by use of approximate techniques such as geometrical optics, billiard theory, and paraxial approximation. However, the free spectral range (FSR) of large cavities, which is inversely proportional to the cavity size, is limited to 0.1–10 nm.[9,11] Furthermore, the weak optical confinement means that they are not very suitable for spontaneous emission control in laser applications.[4]

Therefore, for future wavelength-division-multiplexed (WDM) systems, very compact microcavity resonators with a wide FSR and the potential for high-density integration and the accommodation of many channels are highly desirable. Modern nanofabrication techniques allow fabrication of very small (1.5–5 μm in diameter) passive and active high-index-contrast semiconductor microcavities with large mode spacing and low threshold

currents.[3–5] Such nanoscale microresonator structures are promising candidates for WDM integrated components with very high packing density and offer potential advantages in performance, size, and cost. However, accurate simulation and optimization of such wavelength-scale high-confinement cavities of various shapes calls for fast, robust, and flexible algorithms based on the rigorous formulation of scattering or eigenvalue problems.

Despite being flexible simulation tools, popular numerical techniques such as finite-difference methods or finite-element methods have several major drawbacks in the present context. Optical microcavities are often placed into infinite space domains, in which case a discretization of the problem requires large computational and memory resources and can lead to errors caused by nonphysical backreflections from the edge of the computational window. Furthermore, for complicated geometrical shapes, staircasing errors may play a significant role in the accuracy of the resulting solution. In this paper we present an efficient full-wave analysis of arbitrary-shape optical microcavities on the basis of the boundary integral equation (BIE) technique. The advantage of the BIE formulation is that the problem is moved from the open infinite domain to a finite one (the contour of the cavity), thus reducing the required computational effort. The use of artificial absorbers at the edge of the computational window is avoided by a proper choice of the kernel (Green's) functions satisfying the radiation condition at infinity. All this leads to very efficient numerical algorithms.

However, BIEs need a certain caution in their imple-

mentation. To reduce the original scattering or eigenvalue problem to a set of coupled BIEs, one can either apply the Green's second identity to the field functions and the Green's functions[9] or, alternatively, use single- or double-layer surface-potential field representations.[2,6] Both procedures lead to the so-called elementary integral equations, which are known to have nonunique solutions at a countable set of real-valued defect frequencies f_i^*.[9,13–15] For wavelength-scale bodies such frequencies are widely spaced and, in many cases, can be distinguished from physical resonant frequencies, and thus elementary integral equations can still be used as an accurate simulation tool.[2,6,9,16] However, it can be shown[13,16] that the integral operators are not only singular at $f = f_i^*$ but also ill conditioned for values of f in a domain around f_i^*. The width of this domain is determined by the complexity of the problem and the accuracy of the numerical scheme. Moreover, the larger the cavity and/or the higher the operational frequency, the smaller the distance between unknown defect frequencies. All the aforementioned problems make the use of elementary integral equations for modeling and especially optimization purposes at best questionable.

Though various formulations of uniquely solvable improved BIEs have been developed for acoustic and microwave scattering problems,[14–17] their applications to the analysis of optical components have been limited.[18,19] The most promising of the improved BIE formulations is the one derived first by Muller[20] and used later by several other authors.[14,21,22] The merit of the set of Muller integral equations (MIEs) is twofold: First, they are free of defects related to the loss of uniqueness, and, second, they have smooth or integrable kernels and thus are of the Fredholm second kind. Once formulated, MIEs have to be solved numerically for all but a few canonical structures. Among the most popular discretization techniques are the Galerkin and collocation methods.[23,24] Since MIEs are the Fredholm second-kind equations, any discretization technique should work well. However, as one of the kernels of the MIEs is singular, special care should be taken when a discretization scheme is applied because the accuracy of the singular integral evaluation is crucial for the convergence rate of the algorithm and overall accuracy of the numerical solution. Furthermore, the presence of high-Q resonances, which are a dominant feature in the electromagnetic field behavior in dielectric cavities, can affect the accuracy of the numerical algorithm. A failure of a local-basis discretization method and finite-difference time-domain (FDTD) techniques to reproduce high-Q resonances in dielectric cavities has been reported,[25,26] especially for high-contrast scatterers.

In this paper we discretize MIEs with the global trigonometric Galerkin basis. We decompose each of the integral operators into a sum of a main part given by the explicit Fourier representation and the remaining part with a smooth kernel that is integrated numerically. Such a procedure leads to the exponentially fast convergence of the solution,[27] in contrast to the polynomial convergence rates of the finite-difference method, finite-element method, or collocation method. We study the performance of the developed algorithm and demonstrate its application by analyzing the resonant spectra of several types of dielectric microcavities used in modern optical WDM systems.

2. PROBLEM FORMULATION

Consider a two-dimensional (2-D) arbitrary-shape homogeneous dielectric cavity with complex medium parameters ε_c, μ_c as shown in Fig. 1. An original three-dimensional microcavity problem was converted into an equivalent 2-D formulation in the $x-y$ plane by use of the effective-index method.[4] Experiments show that the electric field of a mode in an optical microdisk cavity is mostly either perpendicular to the plane of the microdisk (TM mode) or lies in the disk plane (TE mode). Thus we assume that the microdisk modes have the same spatial dependence in the vertical direction as guided modes of an equivalent slab waveguide at the same frequency (see Fig. 2). The propagation constant of the corresponding TE- or TM-guided mode of the slab was used as an effective refractive index of the cavity in the following 2-D computations.

For simplicity of formulation, the external region is considered to be uniform and is characterized by the complex medium parameters ε_e, μ_e, though the method can
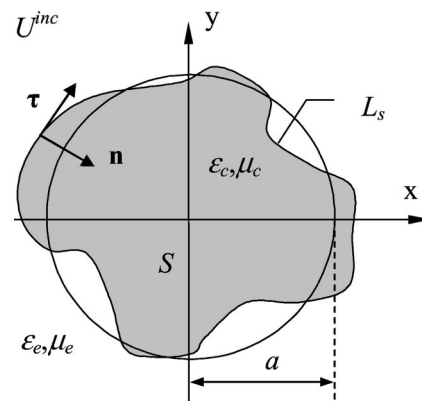

Fig. 1. Geometry of the problem. Shaded area S is the cross section of an optical microcavity with parameters ε_c and μ_c, enclosed by an arbitrary smooth simple contour L_S. A canonical circular contour of radius a and global and local coordinate systems are also shown.
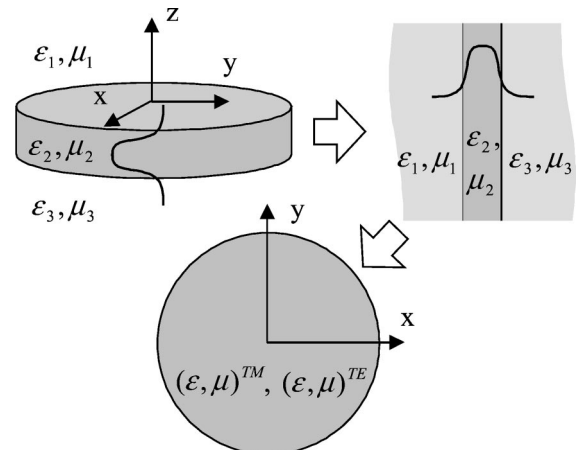

Fig. 2. Two-dimensional model of the microdisk with the effective refractive-index approximation for TE and TM polarizations.

easily be generalized to consider layered dielectric media.[2,6,28] The total field can be characterized by a single scalar function U, which represents either the E_z or the H_z component for the case of TM or TE polarization, respectively. The whole space is separated into two homogeneous regions (several regions if multiple microcavities are considered), and in each region the function U is written as follows:

$$U(\vec{r}) = \begin{cases} U^0(\vec{r}) + U^e(\vec{r}), & \vec{r} \notin S \\ U^c(\vec{r}), & \vec{r} \in S \end{cases} \quad (1)$$

where $U^0(\vec{r})$ either represents the field generated by exterior sources or should be assumed zero if eigenfrequencies of the microcavity are being sought.

For the uniqueness of the solution, the total field must satisfy the following conditions: (1) the Helmholtz equation with the coefficients $k_c^2 = \varepsilon_c \mu_c k^2$ and $k_e^2 = \varepsilon_e \mu_e k^2$ inside and outside the cavity, respectively; (2) a set of continuity conditions on L_S that characterizes a transparent boundary:

$$(U^e + U^0)|_{L_S} = U^c|_{L_S}, \quad \frac{1}{\alpha_c} \frac{\partial U^c}{\partial n}\bigg|_{L_S}$$

$$= \frac{1}{\alpha_e} \left(\frac{\partial U^e}{\partial n} + \frac{\partial U^0}{\partial n} \right)\bigg|_{L_S}; \quad (2)$$

and (3) the Sommerfeld radiation condition for the scattered field at $r = (x^2 + y^2)^{1/2} \to \infty$. Here $k = \omega/c$ (ω is the angular frequency, and c is the light velocity in the vacuum); $\partial/\partial n$ is the normal derivative; $\boldsymbol{\tau}$ and $\mathbf{n}$ are the tangential and inward normal unit vectors to L_S at the point $\mathbf{r}$, respectively; and the coefficient α_j is equal to either μ_j in the TM-polarization case or ε_j in the TE-polarization case ($j = e$ or c). Time dependence is adopted as $\exp(-i\omega t)$ and omitted throughout the paper.

3. BOUNDARY INTEGRAL EQUATIONS

A. Muller Integral Equation Formulation

The integral representations for the fields in each region can be obtained by applying the Green's second identity to the field function at the contour of the dielectric scatterer and the corresponding Green's function,

$$U^c(\mathbf{r}) = \int_{L_S} \left[U^c(\mathbf{r}') \frac{\partial G_c(\mathbf{r}, \mathbf{r}')}{\partial n'} \right.$$

$$\left. - \frac{U^c(\mathbf{r}')}{\partial n'} G_c(\mathbf{r}, \mathbf{r}') \right] dl', \quad \mathbf{r} \in S, \quad (3)$$

$$U^e(\mathbf{r}) = \int_{L_S} \left[\frac{U^e(\mathbf{r}')}{\partial n'} G_e(\mathbf{r}, \mathbf{r}') \right.$$

$$\left. - U^e(\mathbf{r}') \frac{\partial G_e(\mathbf{r}, \mathbf{r}')}{\partial n'} \right] dl'$$

$$+ U^0(\mathbf{r}), \quad \mathbf{r} \notin S, \quad (4)$$

where dl' is an elementary arc along L_S, and the expressions for the 2-D Green's functions and their derivatives can be found in Appendix A. By placing the observation

point at the contour, $\vec{r} \in L_S$, one obtains a pair of coupled BIEs that can be solved numerically.[9] However, the solution of this set is not unique, and if the frequency of the incident field coincides with defect frequencies of the structure, undesired spurious resonances appear. To avoid this problem, we reformulate the problem in terms of a set of the second-kind MIEs. To this end, we add two BIEs formulated in the regions inside and outside the cavity, and their normal derivatives, and impose the boundary conditions [Eqs. (2)] to obtain the following set of coupled integral equations:

$$\phi(\mathbf{r}) - \int_{L_S} \left[\phi(\mathbf{r}') \left(\frac{\partial G_c}{\partial n'} - \frac{\partial G_e}{\partial n'} \right) \right.$$

$$\left. - \psi(\mathbf{r}') \left(G_c - \frac{\alpha_c}{\alpha_e} G_e \right) \right] dl' = U^0(\mathbf{r}), \quad (5)$$

$$\frac{\alpha_e + \alpha_c}{2\alpha_c} \psi(\mathbf{r}) - \int_{L_S} \left[\phi(\mathbf{r}') \left(\frac{\partial^2 G_c}{\partial n \partial n'} - \frac{\partial^2 G_e}{\partial n \partial n'} \right) - \psi(\mathbf{r}') \right.$$

$$\left. \times \left(\frac{\partial G_c}{\partial n} - \frac{\alpha_c}{\alpha_e} \frac{\partial G_e}{\partial n} \right) \right] dl' = \frac{\partial U^0(\mathbf{r})}{\partial n}. \quad (6)$$

Here the unknowns $\phi(\mathbf{r})$ and $\psi(\mathbf{r})$ are the limit values of the field function and its normal derivative, respectively, if approaching the contour L_S from the inner region of the cavity. Equations (5) and (6) are the classical BIEs of the Fredholm second kind, which are uniquely solvable for any incident field function twice continuous on L_S. Note that the kernels of MIEs tend to zero if the contrast between the cavity and the outer medium gets smaller. Therefore one can conclude that the MIE technique relates to the family of the analytical regularization methods[29] based on the inversion of the low-contrast limit form of BIEs.

Having solved the set of Eqs. (5) and (6), we can compute the far-field scattering characteristics as well as the near-field portraits. Large-r evaluation of the integral in the expression for the scattered field [Eq. (4)] reduces it to $U^e(\mathbf{r}) = (1/r)^{1/2} \exp(ik_e r)\Psi(\theta)$. Here the last factor is the far-field scattering pattern given as

$$\Psi(\theta) = \frac{1 + i}{4\sqrt{\pi k_e}} \int_{L_S} \left\{ i\mathbf{k}_\theta \mathbf{n}' \cdot [\phi(\mathbf{r}') - U^0(\mathbf{r}')] \right.$$

$$\left. - \left[\psi(\mathbf{r}') - \frac{\partial U^0(\mathbf{r}')}{\partial n'} \right] \right\} \exp(-i\mathbf{k}_\theta \mathbf{r}') dl', \quad (7)$$

where $\mathbf{k}_\theta = \{k_e \cos\theta, k_e \sin\theta\}$ and θ is the observation angle. The total scattering cross section is then defined as follows:

$$\sigma_s = \frac{2}{\pi} \int_0^{2\pi} |\Psi(\theta)|^2 d\theta. \quad (8)$$

A partial verification of the numerical solution can be done by checking the power conservation law, which for the case of a lossless microcavity illuminated by a plane wave incident at an angle γ takes the following form: $\sigma_s = -8\pi \operatorname{Re}[\Psi(\gamma)]$.

B. Trigonometric–Trigonometric Galerkin Method

To obtain a discrete form of the MIEs (5) and (6), we apply a Galerkin method with angular exponents as global test and trial functions, known as the trigonometric–trigonometric Galerkin method. It has been demonstrated[2,6,27,29] that successful implementation of such a technique strongly depends on the specific Fourier representation of the discretized integral operator. If the operator decomposes into a main part that has an explicit Fourier representation and a remaining part, that is an integral operator with a smooth kernel, then the application of the trigonometric Galerkin method yields discrete numerical schemes with optimal convergence rates. Although the integral operators in Eqs. (5) and (6) do not have such convolutional parts *a priori*, they can be decomposed into two parts: the same operators defined on a circular contour of radius a and the ones obtained as differences between the original and the circular-case operators. If applied to the discretization of the singular BIEs of the first kind, this procedure enables one to treat the singularities analytically and regularize BIEs by converting them into a Fredholm second-kind block-matrix equation.[2,6,29]

For brevity, we present the details of the discretization procedure for the case of the TM-polarized plane-wave scattering from a microcavity with a dielectric permittivity ε_c, assuming that $\mu_c = \mu_e = 1$. If the curve L_s has an analytical parameterization, $x = x(s)$, $y = y(s)$, and $0 \leqslant s \leqslant 2\pi$, the set of Eqs. (5) and (6) can be rewritten as follows:

$$\phi(s) = \int_0^{2\pi} [\, \phi(s')(s, s') - \psi(s')B(s, s')]L(s')\mathrm{d}s'$$
$$+ U^0(s), \tag{9}$$

$$\psi(s) = \int_0^{2\pi} [\, \phi(s')C(s, s') - \psi(s')D(s, s')]L(s')\mathrm{d}s'$$
$$+ \frac{\partial U^0(s)}{\partial n}, \tag{10}$$

where $A(s, s') = \partial F(s, s')/\partial n'$, $B(s, s') = F(s, s')$, $C(s, s') = \partial^2 F(s, s')/\partial n\,\partial n'$, $D(s, s') = \partial F(s, s')/\partial n$, $F(s, s') = G_c(s, s') - G_e(s, s')$, and $L(s) = [(\mathrm{d}x/\mathrm{d}s)^2 + (\mathrm{d}y/\mathrm{d}s)^2]^{1/2}$. Using the small-argument approximations of the cylindrical functions, it can be proved[6] that the function $F(s, s')$ and its first-order normal derivatives are regular functions if L_S is smooth. The second-order normal derivative, however, has a logarithmic singularity at $s = s'$:

$$\lim_{s \to s'} \frac{\partial^2 F(s, s')}{\partial n\,\partial n'} = \frac{k^2}{4\pi}[\varepsilon_e \ln(k_e R) - \varepsilon_c \ln(k_c R)].$$
$$\tag{11}$$

To obtain a discrete form of Eqs. (9) and (10) and simultaneously evaluate the log-singular integral analytically, we first add and subtract to each of the operators $A(s, s')$ to $D(s, s')$ the same operators defined on the circular contour of radius a, $A^0(s, s')$ to $D^0(s, s')$ (see Appendix A). Expanding all the functions in Eqs. (9) and (10) in terms of the Fourier series with angular exponents as global basis functions as

$$L(s)\phi(s) = \frac{2}{i\,\pi k}\sum_{(m)} \phi_m \exp(ims),$$

$$L(s)\psi(s) = \frac{2}{i\,\pi}\sum_{(m)} \psi_m \exp(ims) \tag{12}$$

and testing against the same set of functions yield the following set of linear algebraic equations:

$$a_m^{11}\phi_m + a_m^{12}\psi_m + \sum_{(n)} (\phi_n A_{mn}^{11} + \psi_n A_{mn}^{12}) = e_m^1, \tag{13}$$

$$a_m^{21}\phi_m + a_m^{22}\psi_m + \sum_{(n)} (\phi_n A_{mn}^{21} + \psi_n A_{mn}^{22}) = e_m^2, \tag{14}$$

where

$$a_m^{11} = \sqrt{\varepsilon_c}J_m^c H_m^{c\,'} - \sqrt{\varepsilon_e}J_m^{e\,'}H_m^e,$$
$$a_m^{12} = J_m^c H_m^c - J_m^e H_m^e,$$
$$a_m^{21} = \varepsilon_e J_m^{e\,'}H_m^{e\,'} - \varepsilon_c J_m^{c\,'}H_m^{c\,'},$$
$$a_m^{22} = \sqrt{\varepsilon_e}J_m^e H_m^{e\,'} - \sqrt{\varepsilon_c}J_m^{c\,'}H_m^c, \tag{15}$$

with $J_m^j = J_m(k_j a)$ and $H_m^j = H_m^{(1)}(k_j a)$ as the Bessel and Hankel functions, respectively, and the prime representing the derivative with respect to the argument. The matrix coefficients are defined as follows:

$$A_{mn}^{11} = -A_{mn}/k - 2(1 - \delta_{m,n})L_{m-n}/i\,\pi k,$$
$$A_{mn}^{12} = B_{mn},$$
$$A_{mn}^{21} = -C_{mn}/k^2,$$
$$A_{mn}^{22} = D_{mn}/k - 2(1 - \delta_{m,n})L_{m-n}/i\,\pi k, \tag{16}$$

where $\delta_{m,n}$ is the Kronecker delta function. Note that all the functions expanded into the double Fourier series are constructed as the differences between the original kernels and the circular-case ones and thus are regular at $s = s'$:

$$A_{mn} = \frac{1}{i\,\pi^2}\int_0^{2\pi}\int_0^{2\pi} [A(s, s')$$
$$- A^0(s, s')]\exp(-ims)\exp(ins')\mathrm{d}s\,\mathrm{d}s'. \tag{17}$$

The right-hand functions are defined as one-dimensional integrals,

$$e_m^1 = \frac{1}{2\pi}\int_0^{2\pi} U^0(s)\exp(-ims)\mathrm{d}s,$$

$$e_m^2 = \frac{1}{2\pi}\int_0^{2\pi} \frac{\partial U^0(s)}{\partial n}\exp(-ims)\mathrm{d}s,$$

$$L_m = \frac{1}{2\pi}\int_0^{2\pi} \frac{\exp(-ims)}{L(s)}\mathrm{d}s, \tag{18}$$

and together with 2-D integrals in Eq. (17) have to be evaluated numerically. Finally, by introducing new unknowns, $z_m^1 = a_m^{11}\phi_m + a_m^{12}\psi_m$ and $z_m^2 = a_m^{21}\phi_m + a_m^{22}\psi_m$, Eqs. (13) and (14) are reduced to the following

final canonical form, a 2×2 block-type infinite-matrix equation of the Fredholm second kind:

$$\begin{pmatrix} \mathbf{z}^1 \\ \mathbf{z}^2 \end{pmatrix} + \begin{bmatrix} \mathbf{M}^{11} & \mathbf{M}^{12} \\ \mathbf{M}^{21} & \mathbf{M}^{22} \end{bmatrix} \times \begin{pmatrix} \mathbf{z}^1 \\ \mathbf{z}^2 \end{pmatrix} = \begin{pmatrix} \mathbf{e}^1 \\ \mathbf{e}^2 \end{pmatrix}. \qquad (19)$$

The existence as well as the uniqueness of the solution of Eq. (19) is guaranteed, and the accuracy can be controlled by changing the size of the truncated matrix.

4. DETAILS OF COMPUTATIONS AND CONVERGENCE ANALYSIS

A. Matrix Truncation Error

The Fredholm nature of the final block-matrix equation (19) guarantees that the computational error of the approximate solution can be progressively minimized by increasing the matrix truncation number N. However, it is important to see what the rate of the error decrease is and its dependence on the microcavity material and geometrical parameters.

The results of the mathematical studies of log-singular integral equations of potential theory show that application of the trigonometric–trigonometric Galerkin technique together with the product integration method guarantees the optimal order convergence rate.[27] As only one equation [Eq. (10)] of our set is (logarithmically) singular, the numerical convergence rate estimate is the same as in the aforementioned studies: If intermediate calculations, like numerical integration, have been performed with "infinite" accuracy, then the approximate numerical solution converges to the exact one exponentially as the truncation number of each block of the matrix is increased. In practice, however, the integrals in Eqs. (17) and (18) are not computed exactly, which leads to the discrete Galerkin method, the convergence of which will be discussed in the following section.

In general, the solution error is defined as $\|z - z^N\|$, where z^N are the unknowns computed by solving Eq. (19) with each block truncated after N equations. As we do not know the exact solution z, we compute the normalized error, in the sense of the l_2^2 norm, between two neighboring solutions versus the block truncation number N:

$$e(N) = \|z^{(N)} - z^{(N+1)}\| \|z^{(N)}\|^{-1},$$

$$\|z^{(N)}\| = \left\{ \sum_{|n| \leqslant N} [|z_n^{1(N)}|^2 + |z_n^{2(N)}|^2] \right\}^{-1/2}. \qquad (20)$$

To study the dependence of the computational error decrement on the problem parameters, we consider a cavity with a super-elliptical cross-sectional contour described by the formula $(x/\mu a_c)^{2\nu} + (y/a_c)^{2\nu} = 1$, where $1 \leqslant \mu < \infty$ is the elongation and $0 < \nu < \infty$ is a corner-sharpness parameter. If $\nu = 1$, the contour becomes an ellipse, and, if $\nu \to \infty$, it turns into a rectangle of sides μa_c and a_c and rounded corners with a peak curvature proportional to ν/a_c.

In Fig. 3(a) we present $e(N)$ graphs computed for the problem of the plane-wave scattering from two ellipses with $\mu = 1.1$ and $\varepsilon_c = 10.24 + 0.001i$, one larger than the other. The error plots are generated for the param-

eters corresponding to the excitation of the whispering-gallery (WG) modes in the cavity: in the $\mathrm{WG}_{4,1}$-mode resonance ($ka_c = 1.845$) and just off this resonance ($ka_c = 1.93$) and in and off the $\mathrm{WG}_{11,1}$-mode resonance ($ka_c = 4.279$ and $ka_c = 4.3$, respectively). One can see that a rapid decrement of the error starts after N becomes larger than the value of a characteristic optical size of the cavity ($k_c a_c$) [Fig. 3(a)], and the rate of this decrement depends strongly on the peak curvature of the corners [Fig. 3(b)]. It is important to study the behavior of the algorithm in the regions of the high-Q cavity resonances, as it has been shown that local-basis discretization methods may fail to provide an acceptable level of accuracy when the same number of unknowns is used as for the off-resonance solution.[25,26] Furthermore, it was observed that the errors in the internal field computation in the region of sharp internal field resonances in the spherical cavity were located mostly on the sphere surface and depended strongly on the refractive index of the cavity.[25] However, as the WG-mode field is mostly located in the area close to the cavity surface, a high accuracy of the field computation in this region is highly desirable. The results shown in Fig. 3(a) convincingly demonstrate that our algorithm converges rapidly in the high-Q cavity resonances. We have also computed a matrix condition number as a function of the problem size and observed that it does not grow with the increase of N but tends to a constant limit value N_{cond} as $N \to \infty$. This limit value depends on the problem parameters and is larger for cavities with sharper corners. For the parameters of Fig. 3(b), it was as follows: $N_{\mathrm{cond}} = 163$ ($\nu = 1$), $N_{\mathrm{cond}} = 222$ ($\nu = 3$), and $N_{\mathrm{cond}} = 323$ ($\nu = 5$). Our experiments with local-basis (pulse, linear, and second-order polynomial) discretization schemes[23] have shown much slower convergence rates with noticeably worse convergence for the resonance than the off-resonance points.
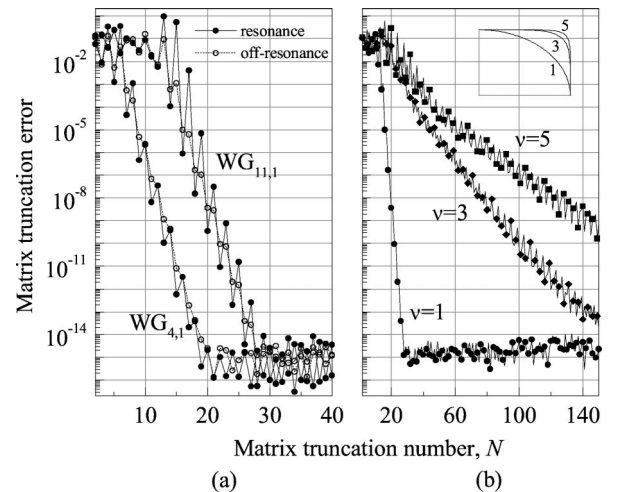

Fig. 3. Computational errors versus truncated matrix size for a TM-polarized plane-wave scattering from a superelliptic microcavity with parameters $\mu = 1.1$ and $\varepsilon_c = 10.24 + 0.001i$: (a) the error in and off two WG-mode resonances of an elliptic ($\nu = 1$) cavity, $ka_c(\mathrm{WG}_{4,1}) = 1.845$ and $ka_c(\mathrm{WG}_{11,1}) = 4.279$; (b) the error for three superelliptic cavities ($ka_c = 4.3$) for various values of the corner-sharpness parameter (corners are shown in the inset).

B. Fast-Fourier-Transform Algorithm for the Computation of Matrix Elements

In the practical implementation of the algorithm, there are other sources of computational errors besides the matrix truncation. As follows from Eq. (17), the matrix elements in Eq. (19) are calculated as double integrals over the interval $[0, 2\pi]$, which is the most time-consuming part of the algorithm. For a standard Galerkin method, converting the BIEs into a dense $N \times N$ matrix has a computational complexity of the order N^3. However, the use of exponential basis and testing functions has an important computational merit. It enables us to calculate matrix elements with the aid of the fast Fourier transform (FFT), thus reducing the computation complexity of the algorithm and hence CPU time. In this case the total number of multiplications in performing a 2-D FFT for an N-unknowns problem does not exceed $N^2 \log_2 N$. Furthermore, as it has been demonstrated in subsection 4.A., owing to the exponential convergence of the method, N can be chosen to be small. To achieve higher accuracy, we combine the FFT algorithm with higher-order Gauss–Legendre quadratures.[30] Thus the Fourier coefficients of a function $f(s)$ are evaluated as

$$
\begin{aligned}
f_m &= \frac{1}{2\pi} \int_0^{2\pi} f(s) \exp(-ims) \mathrm{d}s \\
&\approx \frac{1}{2M} \sum_{l=1}^{Q} w_l \exp(-im\hat{s}_l) \\
&\quad \times \sum_{n=0}^{M-1} f\left(\hat{s}_l + \frac{2\pi n}{M} \right) \exp\left(-\frac{2i\pi mn}{M} \right),
\end{aligned}
\tag{21}
$$

where $\hat{s}_l = \pi(s_l + 1)/M$ and s_l, w_l denote the abscissas and weights, respectively, for the Gaussian quadrature on the interval $[-1, 1]$ with Q nodal points. The last sum in expression (21) is computed with the FFT algorithm.

C. Overall Convergence Rate

According to Ref. 31, we have the following estimate for the N-unknowns final approximate solution after the numerical integration has been performed: $\|z - z^{(N)}\| \leqslant \mathrm{const}\, N^{-d-1}$, where d is a degree of precision of the numerical quadrature. However, small values of N acceptable for a projection scheme are always smaller than the FFT size M required for an acceptable level of aliasing errors. Therefore in practical computations we use an FFT of size $M > N$ and then truncate the result. Finally, we can conclude that, though a final fully discretized scheme does not have the exponential convergence rate, this rate can be progressively improved by increasing the order of the Gaussian quadrature.

The error estimate for the local-basis Galerkin method by use of test and trial functions that are polynomials of degree p and a numerical quadrature of degree d is as follows: $\|z - z^{(N)}\| \leqslant \mathrm{const}(N^{-d-1} + N^{-p})$.[31] This estimate shows that to maintain the accuracy of the Galerkin method, an integration technique accurate to the order of the error in the discretization scheme must be employed. On the other hand, it can be seen that it is pointless to increase d to a value higher than $p - 1$, since the overall convergence rate is limited by the order of the test and trial functions used. This represents the most serious limitation to achieving arbitrary accuracy with standard local-basis discretization algorithms.

5. NUMERICAL SIMULATIONS

When studying dielectric and semiconductor microcavities for laser and integrated optics applications, we are interested in computing the spectrum of natural modes supported, together with the mode's near- and far-field distributions, Q factors, and FSR. These characteristics enable one to estimate and tune practical design and performance parameters such as laser pump threshold, maximum output power, emission directionality, filter operational frequencies, efficiency of coupling to bus waveguides, and single- or multimode operation within an optical communications window. For achieving a single-mode operation at a 1.55-μm wavelength, an FSR of the microcavity larger than the 30-nm-wide optical communications window supported by erbium-doped amplifiers is required. This calls for the use of very small (1–5-μm radius) semiconductor microcavities. Thus in this section we study the characteristics of several 1–5-μm-sized high-confinement optical microcavities frequently used as compact filters and laser resonators in dense WDM systems in the 1.55-μm wavelength band.

To study the optical spectra of microcavities, one can excite them by the 2-D complex-source-point (CSP) beam.[32] CSP is a line field source with complex coordinates: $U^{\mathrm{inc}} = H_0^{(1)}(k|\mathbf{r} - \mathbf{r}_{cs}|)$, $\mathbf{r}_{cs} = \{x_{cs}, y_{cs}\} = \mathbf{r}_0 + i\mathbf{b}$, $\mathbf{r}_0 = \{x_0, y_0\}$, and $\mathbf{b} = \{b \cos \beta, b \sin \beta\}$. Such a source produces a beam field in real space, and the greater the imaginary part of the source coordinate, the narrower the beam. This field is an exact solution of the Helmholtz equation at any observation point, unlike the Gaussian-type exponents frequently used to approximate the beam fields in paraxial domains. For each cavity, the beam incident angle and/or a separation between the beam center and a cavity sidewall (beam impact parameter) have been tuned to achieve the most efficient coupling into the highest-Q cavity modes.

Before applying our method to the analysis of general microcavity shapes, we verify our results by comparing them with data obtained by other methods, keeping a uniform accuracy of computations of 10^{-4}. As a first test example, we chose a circular microdisk. Not only is such a structure used in many practical optoelectronic applications, but also its 2-D equivalent problem has an analytical solution as a series of cylindrical functions. A frequency scan of the total scattered power of the TE-polarized CSP beam field from a circular microcavity with a radius $a_c = 1.5\ \mu$m and permittivity $\varepsilon_c = 6.0614 + 0.001i$ is shown in Fig. 4. The values of the total scattered power are normalized to the power of the free-space CSP beam. The minima in the plot (cavity resonances) are observed owing to the absorption of the beam energy in the cavity material when the frequency of the incident beam coincides with the real part of the cavity's complex natural frequency. To keep the formulation general, the radius of the extracted circular contour in the MIEs algorithm implementation was chosen to be different from the radius of the circular cavity under analysis ($a \neq a_c$). In
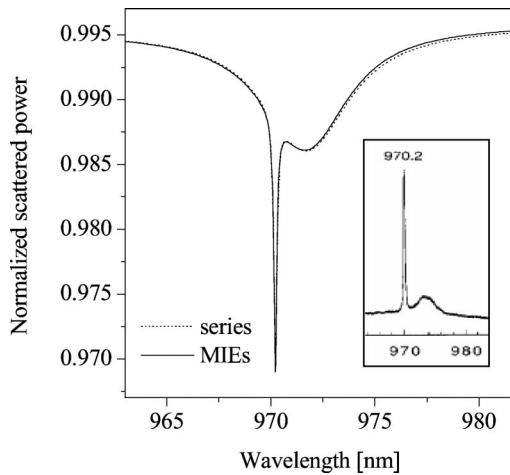
Fig. 4. Validation of the MIEs solution: comparison of results generated by the MIEs with the analytical solution and experimental data. The inset shows an emission spectrum of an optically pumped GaAs microdisk 3 μm in diameter and 90 nm in thickness [Ref. 33, Fig. 2(b)]. The effective refractive index used in the 2-D computations was taken as $n_c = 2.462$.

the wavelength range of 963–982 nm, we observe one sharp minimum and one wide minimum corresponding to the excitation of two WG modes of different Q factors in the microcavity. A very good agreement of the results with the series solution is demonstrated for all points of the graph, including the sharp resonance position and depth. The inset shows the measured emission spectra of a 3-μm-diameter and 90-nm-thick GaAs microdisk.[33] The wavelength of the sharp peak was measured to be 970.2 nm, and the corresponding value in our 2-D calculations was 970.24 nm. A small difference in the resonance position is likely due to an effective-index approximation of the original three-dimensional problem.

As a second example, we study a microgear cavity studied numerically by the FDTD method[7,8] and then experimentally.[34] The microgear cavity is essentially a circular microdisk with a sinusoidal corrugation of the disk radius that can be described parametrically as follows: $r(s) = a_c[1 + \delta \sin(\nu s)]$. Here a_c is a radius of an unperturbed circular cavity, ν is a corrugation period, and δ is the relative corrugation amplitude. Such a specific contour deformation allows efficient splitting of a double-degenerate $WG_{n,1}$ WG mode of the microdisk, for which the number of the azimuthal field variations is $n = \nu/2$, as well as enhancing a lasing mode and suppressing a parasitic mode.[7,8,32] Owing to many variations of the contour, numerical results obtained by FDTD techniques may suffer from staircasing errors, and the BIE method appears to be an optimal computer-aided-design tool providing higher accuracy with less computational effort.

The complex natural wavelengths ($\tilde{\lambda} = \lambda + i\lambda'$) of the microcavities were found as the wavelengths at which the determinant of the block matrix [Eq. (19)] vanishes. Once the mode's natural wavelength is found, the modal-field distribution can be computed, and the Q factor can be obtained as follows: $Q = \lambda/2\lambda'$. In Fig. 5 we show the resonant wavelengths and Q factors (curves) of TE-polarized $WG_{5,1}^{\pm}$ modes as a function of the corrugation amplitude δ for the InGaAs–InGaAsP microgear cavity[7]

with radius $a_c = 0.8$ μm, thickness $h = 0.18$ μm (effective refractive index $n_{\rm eff} = 2.63$), and $\nu = 10$. The wavelengths and Q factors are normalized to the unperturbed circular-microdisk wavelength λ_c and Q factor, respectively. The results obtained by the 2-D FDTD technique[7] are plotted for comparison (circles). It can be clearly seen that the algorithm based on MIEs enables us to demonstrate a continuous shift of the microcavity's lasing wavelengths and Q factors with a continuous change of the relative corrugation amplitude, whereas the FDTD results experience some nonphysical fluctuations. Similar fluctuational behavior has been observed in the FDTD simulations of the microgear cavity.[8]

Next, we study resonant spectra, the FSR, and modal-field portraits of three popular optical microcavity shapes: an ellipse, a racetrack, and a square. The wavelength dependence of the total scattered power of the TM-polarized CSP beam field from an elliptical microcavity ($x = a_c\mu \cos s$ and $y = a_c \sin s$) with $a_c = 0.95$ μm, $\varepsilon_c = 10.24 + 0.001i$, and $\mu = 1.1$ is shown in Fig. 6. Two families of WG-mode resonances can be seen, corresponding to the first- and second-radial-order modes. The $WG_{n,1}$ have the highest optical confinement and lowest material losses and therefore higher values of the Q factors and lower thresholds. All the higher-radial-order modes are usually considered parasitic, and for certain applications need to be suppressed.[2,6] The near-field portraits, resonant wavelengths, and Q factors of the $WG_{11,1}$ and $WG_{7,2}$ modes are presented in Fig. 7.

Another microcavity shape that finds many applications in integrated optics is a racetrack (quadrupole) resonator[1] with the cross-section contour defined as $x = a_c\mu r(s)$, $y = a_c r(s)$, and $r(s) = [1 + e\cos(2s)]/\sqrt{1 + e^2/2}$. The normalized scattered power of the CSP beam scattering from a racetrack microcavity is shown in Fig. 8. Within the computed wavelength range the highest-Q resonances of this cavity are again first-radial-order WG modes. Along with the WG modes,
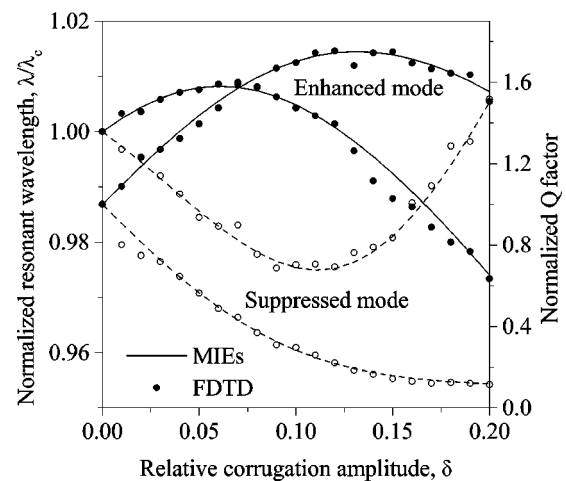

Fig. 5. Normalized wavelengths and Q factors of $WG_{5,1}^{\pm}$ modes of a microgear cavity ($a_c = 0.8$ μm, $n_{\rm eff} = 2.63$, and $\nu = 10$) as a function of relative perturbation amplitude δ. The results are compared with those obtained by the FDTD technique (Ref. 7, Figs. 5 and 6) (circles). Solid curves (filled circles) and dashed curves (open circles) are the results for the enhanced and suppressed modes, respectively.
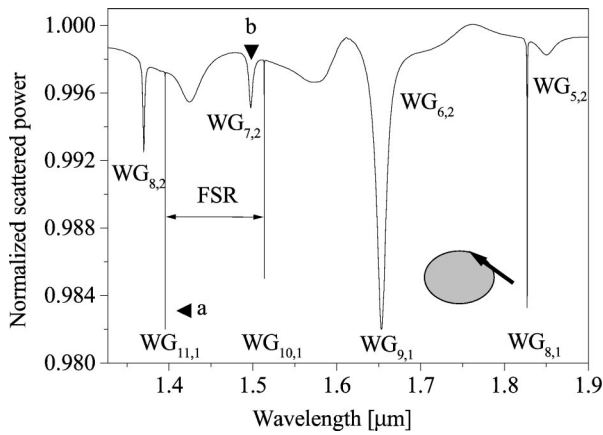
Fig. 6. Wavelength dependence of the total power scattered from an elliptical microcavity (a_c = 0.95 μm, ε_c = 10.24 + 0.001i, and μ = 1.1) excited by a TM-polarized CSP beam. The FSR of the first-radial-order WG-mode resonances in the vicinity of λ = 1.55 μm is 118 nm. The inset shows a schematic of the CSP beam (kb = 10, β = 160°, kx_0 = $ka_c\mu$ + kb + 1, and ky_0 = 0) grazing the rim of the microdisk.
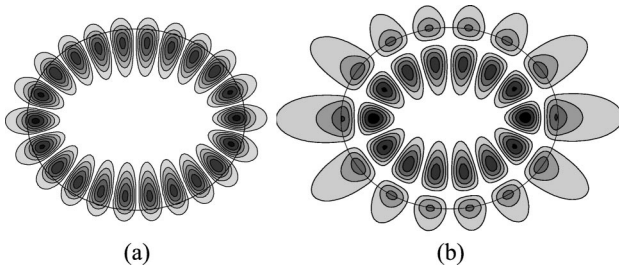

Fig. 7. Near-field intensity patterns (20% contours) of WG modes in the elliptical microcavity. Corresponding resonances in the normalized scattered power in Fig. 6 are marked as a and b. (a) First-radial-order WG$_{11,1}$ mode (λ = 1.395 μm, and Q = 1.01 × 10^4), (b) second-radial-order WG$_{7,2}$ mode (λ = 1.497 μm and Q = 2.91 × 10^2).
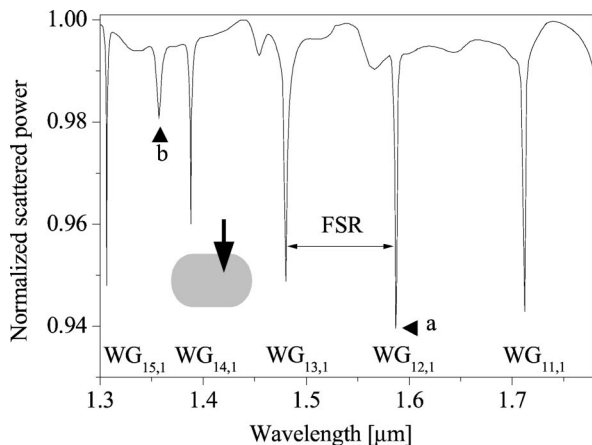

Fig. 8. Wavelength dependence of the total power scattered from a recetrack microcavity (a_c = 1.2 μm, ε_c = 10.24 + 0.001i, e = 0.15, and μ = 1) excited by a TM-polarized CSP beam. The FSR of the first-radial-order WG-mode resonances in the vicinity of λ = 1.55 μm is 106 nm. The inset shows a schematic of the incident CSP beam (kb = 10, β = 270°, kx_0 = ka_c/2, and ky_0 = ka_c + kb + 0.1).

bow-tie resonances are excited in the racetrack microcavity. They demonstrate a strong spatial directionality of the output light that is very important for laser applications.[1] Near-field intensity patterns of a WG mode and a bow-tie mode are presented in Figs. 9(a) and 9(b), respectively.

Finally, the wavelength dependence of the total scattered power for a CSP beam incident at an angle β = 45° to the sidewall of a square microcavity is plotted in Fig. 10. The square shape of the microcavity has been approximated by the superelliptic parametric formula: $x = a_c\mu \cos sr(s)$, $y = a_c \sin sr(s)$, and $r(s) = (|\cos s|^{2\nu} + |\sin s|^{2\nu})^{-1/2\nu}$. A square resonator supports standing-wave modes of various types, as previously observed,[12] and the highest-Q factor modes are the ones having the nulls of the electric field along the diagonals [Fig. 11(a)]. It can be seen that though the mode spacing of the highest-Q modes is rather large, the spectrum of the resonances corresponding to the modes of different types [see
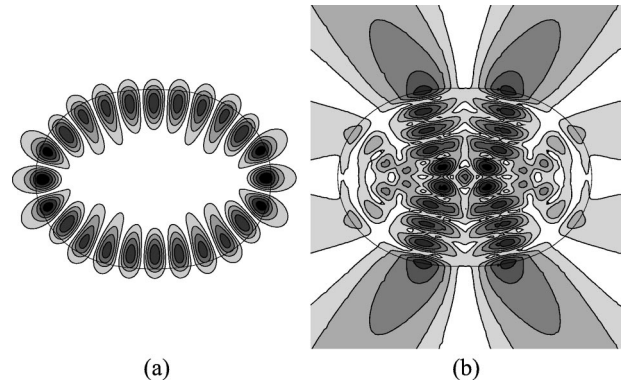

Fig. 9. Near-field intensity patterns (20% contours) of (a) WG and (b) bow-tie modes in the racetrack microcavity. Corresponding resonances in the normalized scattered power in Fig. 8 are marked as a and b. (a) First-radial-order WG$_{12,1}$ mode (λ = 1.587 μm and Q = 1.32 × 10^3), (b) bow-tie WG$_{7,2}$ mode (λ = 1.357 μm and Q = 2.66 × 10^2).
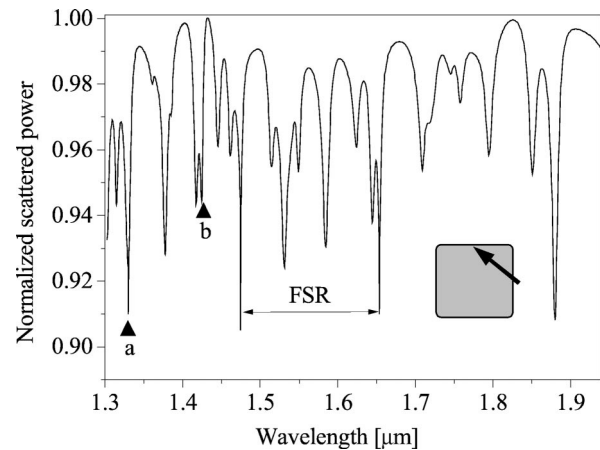

Fig. 10. Wavelength dependence of the total power scattered from a square microcavity (a_c = 1.45 μm, ε_c = 10.24 + 0.001i, ν = 10, and μ = 1) excited by a TM-polarized CSP beam. The FSR in the vicinity of λ = 1.55 μm is 178 nm. The inset shows a schematic of the incident CSP beam (kb = 10, β = 135°, kx_0 = ka_c + kb + 0.1, and ky_0 = 0).
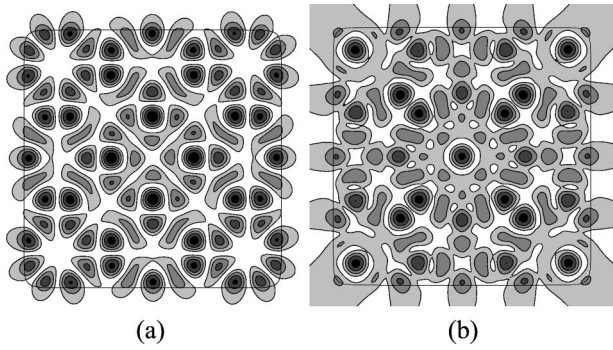
Fig. 11. Near-field intensity patterns (20% contours) of the modes in the square microcavity corresponding to the resonances in the normalized scattered power marked as a and b in Fig. 10. (a) ($\lambda = 1.33\ \mu m$ and $Q = 3.48 \times 10^3$), (b) ($\lambda = 1.425\ \mu m$ and $Q = 5.41 \times 10^2$).

Fig. 11(b) as an example] is very dense. This suggests that to achieve a single-mode operation of the square microcavity one should either decrease the size of the cavity even further or introduce a deformation to suppress the parasitic cavity modes.

6. CONCLUSIONS

A set of boundary integral equations for calculating optical modes in high-confinement resonant cavities has been used. The BIEs are guaranteed to have a unique solution for any set of cavity design parameters unlike various elementary formulations suffering from the appearance of spurious numerical resonances. The BIEs have been discretized by the Galerkin method with global trigonometric test and trial basis functions to minimize the size of the numerical problem and achieve the stability and superior convergence of the final fully discrete numerical scheme. The algorithms developed have enabled us to accurately and efficiently compute the characteristics of arbitrary-shape lossy dielectric and semiconductor microcavities with various types of excitation. Our results were found to be in good agreement with FDTD simulations available in the literature and shown to provide higher accuracy. The speed, flexibility, and robustness of the algorithms create a framework for efficient design and optimization of novel-shape microcavities with improved spectral characteristics.

APPENDIX A: TWO-DIMENSIONAL GREEN'S FUNCTION AND ITS DERIVATIVES

The 2-D Green's function of the uniform medium with parameters ε_j, μ_j and its first- and second-order normal derivatives is as follows:

$$\partial G_j(\mathbf{r}, \mathbf{r}') = \frac{i}{4} H_0^{(1)}(k_j R), \tag{A1}$$

$$\frac{\partial G_j(\mathbf{r}, \mathbf{r}')}{\partial n} = -\frac{ik_j}{4} H_1^{(1)}(k_j R) \frac{\partial R}{\partial n}, \tag{A2}$$

$$\frac{\partial^2 G_j(\mathbf{r}, \mathbf{r}')}{\partial n\, \partial n'} = -\frac{i}{4}\left[k_j^2 H_0^{(1)}(k_j R) \frac{\partial R}{\partial n} \frac{\partial R}{\partial n'} + k_j H_1^{(1)}(k_j R) \right.$$
$$\left. \times \left(\frac{\partial^2 R}{\partial n\, \partial n'} - \frac{1}{R} \frac{\partial R}{\partial n} \frac{\partial R}{\partial n'} \right) \right]. \tag{A3}$$

Here $k_j = k\sqrt{\varepsilon_j \mu_j}$; $H_{0(1)}^{(1)}(\,\cdot\,)$ is the zero- (first-) order Hankel function of the first kind; $\mathbf{r}$ and $\mathbf{r}'$ are the vectors from the origin to the observation and source points, respectively; $R = |\mathbf{r} - \mathbf{r}'|$; and $L(s) = [(dx/ds)^2 + (dy/ds)^2]^{1/2}$ is the Jacobian of the contour L_S. The first- and second-order normal derivatives of R are given by

$$\frac{\partial R}{\partial n} = -\frac{1}{L(s)R}\left[\frac{dy}{ds}(x - x') - \frac{dx}{ds}(y - y') \right], \tag{A4}$$

$$\frac{\partial^2 R}{\partial n\, \partial n'} = -\frac{\dfrac{dy}{ds}\dfrac{dy'}{ds'} + \dfrac{dx}{ds}\dfrac{dx'}{ds'}}{L(s)L(s')R} - \frac{1}{R}\frac{\partial R}{\partial n}\frac{\partial R}{\partial n'}. \tag{A5}$$

For the case of the axial-symmetrical problem for a circular cylinder of radius a, the expressions (A1)–(A3) take the following form:

$$G_j^0(s, s') = \frac{i}{4} H_0^{(1)}(2k_j a R_0), \tag{A6}$$

$$\frac{\partial G_j^0(s, s')}{\partial n} = -\frac{ik_j}{4} R_0 H_1^{(1)}(2k_j a R_0), \tag{A7}$$

$$\frac{\partial^2 G_j^0(s, s')}{\partial n\, \partial n_s} = \frac{ik_j^2}{4}\left[\frac{1}{2k_j a} R_0^{-1} H_1^{(1)}(2k_j a R_0) \right.$$
$$\left. - R_0^2 H_0^{(1)}(2k_j a R_0) \right], \tag{A8}$$

where

$$R_0 = \left| \sin \frac{s - s'}{2} \right|.$$

Integral operators with any of the kernel functions (A6)–(A8) have the same set of orthogonal eigenfunctions $\{\exp(ims)\}_{m=-\infty}^{\infty}$, and their Fourier coefficients can be obtained analytically[6,16] in terms of cylindrical functions:

$$\int_0^{2\pi} G_j^0(s, s')\exp(ims')ds' = \frac{i\pi}{2} J_m^j H_m^j \exp(ims), \tag{A9}$$

$$\int_0^{2\pi} \frac{\partial G_j^0(s, s')}{\partial n}\exp(ims')ds'$$
$$= \left(-\frac{1}{2} + \frac{ik_j\pi}{2} J_m^{j'} H_m^j \right)\exp(ims)$$
$$= \left(\frac{1}{2} + \frac{ik_j\pi}{2} J_m^j H_m^{j'} \right)\exp(ims), \tag{A10}$$

$$\int_0^{2\pi} \frac{\partial^2 G_j^0(s, s')}{\partial n \, \partial n'} \exp(ims') \mathrm{d}s'$$

$$= \frac{ik_j^2 \pi}{2} J_m^{j'} H_m^{j'} \exp(ims). \qquad (A11)$$

Here, with $m = 0, \pm 1, ...,$ $J_m^j = J_m(k_j a)$ and $H_m^j = H_m^{(1)} \times (k_j a)$ are the Bessel and first-kind Hankel functions of order m, respectively, and the prime represents the derivative with respect to the argument.

ACKNOWLEDGMENTS

Svetlana V. Boriskina, the corresponding author, can be reached by e-mail at eezsb@gwmail.nottingham.ac.uk.

REFERENCES

1. C. Gmachl, F. Cappasso, E. E. Narimanov, J. U. Nockel, A. D. Stone, J. Faist, D. L. Sivco, and A. Y. Cho, "High-power directional emission from microlasers with chaotic resonances," Science **280**, 1556–1564 (1998).
2. S. V. Boriskina and A. I. Nosich, "Radiation and absorption losses of the whispering-gallery-mode dielectric resonators excited by a dielectric waveguide," IEEE Trans. Microwave Theory Tech. **47**, 224–231 (1999).
3. P. P. Absil, J. V. Hryniewicz, B. E. Little, F. G. Johnson, K. J. Ritter, and P.-T. Ho, "Vertically coupled microring resonators using polymer wafer bonding," IEEE Photon. Technol. Lett. **13**, 49–51 (2001).
4. M. K. Chin, D. Y. Chu, and S.-T. Ho, "Estimation of the spontaneous emission factor for microdisk lasers via the approximation of whispering gallery modes," J. Appl. Phys. **75**, 3302–3307 (1994).
5. M. Fujita, A. Sakai, and T. Baba, "Ultrasmall and ultralow threshold GaInAsP–InP microdisk injection lasers: design, fabrication, lasing characteristics, and spontaneous emission factor," IEEE J. Sel. Top. Quantum Electron. **15**, 673–681 (1999).
6. S. V. Boriskina, T. M. Benson, P. Sewell, and A. I. Nosich, "Tuning of elliptic whispering-gallery-mode microdisk waveguide filters," J. Lightwave Technol. **21**, 1987–1995 (2003).
7. B.-J. Li and P.-L. Liu, "Numerical analysis of microdisk lasers with rough boundaries," IEEE J. Quantum Electron. **35**, 791–795 (1997).
8. M. Fujita and T. Baba, "Proposal and finite-difference time-domain simulation of whispering gallery mode microgear cavity," IEEE J. Quantum Electron. **37**, 1253–1258 (2001).
9. J. Wiersig, "Boundary element method for resonances in dielectric microcavities," J. Opt. A Pure Appl. Opt. **5**, 53–60 (2003).
10. Y.-Z. Huang, W.-H. Guo, and Q.-M. Wang, "Analysis and numerical simulation of eigenmode characteristics for semiconductor lasers with an equilateral triangle microresonator," IEEE J. Quantum Electron. **37**, 100–107 (2001).
11. A. W. Poon, F. Courvoisier, and R. K. Chang, "Multimode resonances in square-shaped optical microcavities," Opt. Lett. **26**, 632–634 (2001).
12. C. Manolatou, M. J. Khan, S. Fan, P. R. Villeneuve, H. A. Haus, and J. D. Joannopoulos, "Coupling of modes analysis of resonant channel add–drop filters," IEEE J. Quantum Electron. **35**, 1322–1331 (1999).
13. D. Colton and R. Kress, *Integral Equations Methods in Scattering Theory* (Wiley, New York, 1983).
14. N. Morita, N. Kumagai, and J. R. Mautz, *Integral Equations Methods for Electromagnetics* (Artech House, London, 1990).
15. A. J. Burton and G. F. Miller, "The application of integral equation methods to the numerical solution of some exterior boundary-value problem," Proc. R. Soc. London Ser. A **323**, 201–210 (1971).
16. S. Amini and S. M. Kirkup, "Solution of Helmholtz equation in the exterior domain by elementary boundary integral methods," J. Comput. Phys. **118**, 208–221 (1995).
17. H. A. Shenk, "Improved integral formulation for acoustic radiation problems," J. Acoust. Soc. Am. **44**, 41–68 (1968).
18. D. W. Prather, M. S. Mirotznik, and J. N. Mait, "Boundary integral methods applied to the analysis of diffractive optical elements," J. Opt. Soc. Am. A **14**, 34–43 (1997).
19. J. M. Bendickson, E. N. Glytsis, T. K. Gaylord, and A. F. Peterson, "Modeling considerations for rigorous boundary element method analysis of diffractive optical elements," J. Opt. Soc. Am. A **18**, 1495–1506 (2001).
20. C. Muller, *Foundations of the Mathematical Theory of Electromagnetic Waves* (Springer-Verlag, Berlin, 1969).
21. V. V. Soloduhov and E. N. Vasiliev, "Diffraction of a plane electromagnetic wave by a dielectric cylinder of arbitrary cross section," Sov. Phys. Tech. Phys. **15**, 32–36 (1970).
22. V. Rokhlin, "Rapid solution of integral equations of scattering theory in two dimensions," J. Comput. Phys. **86**, 414–439 (1990).
23. R. F. Harrington, *Field Computation by Moment Methods* (Krieger, Malabar, Fla., 1968).
24. K. E. Atkinson, *The Numerical Solution of Boundary Integral Equations* (Cambridge U. Press, Cambridge, UK, 1997).
25. A. Hoekstra, J. Rahola, and P. Sloot, "Accuracy of internal fields in volume integral equation simulations of light scattering," Appl. Opt. **37**, 8482–8497 (1998).
26. G. L. Hower, R. G. Olsen, J. D. Earls, and J. B. Schneider, "Inaccuracies in numerical calculation of scattering near natural frequencies of penetrable objects," IEEE Trans. Antennas Propag. **41**, 982–986 (1993).
27. J. Saranen and G. Vainikko, "Trigonometric collocation method with product integration for boundary integral equations on closed curves," SIAM J. Numer. Anal. **33**, 1577–1596 (1996).
28. M. Paulus and O. J. F. Martin, "Light propagation and scattering in stratified media: a Green's tensor approach," J. Opt. Soc. Am. A **18**, 854–861 (2001).
29. A. I. Nosich, "The method of analytical regularization in wave-scattering and eigenvalue problems: foundations and review of solutions," IEEE Antennas Propag. Mag. **41**, 34–49 (1999).
30. U. Lamp, K.-T. Schleicher, and W. L. Wendland, "The fast Fourier transform and the numerical solution of one-dimensional boundary integral equations," Numer. Math. **15**, 15–38 (1985).
31. K. Atkinson and A. Bogomolny, "The discrete Galerkin method for integral equations," Math. Comput. **48**, 595–616 (1987).
32. A. V. Boriskin and A. I. Nosich, "Whispering-gallery and Luneburg-lens effects in a beam-fed circularly layered dielectric cylinder," IEEE Trans. Antennas Propag. **50**, 1245–1249 (2002).
33. H. Cao, J. Y. Xu, W. H. Xiang, Y. Ma, S.-H. Chang, S. T. Ho, and G. S. Solomon, "Optically pumped InAs quantum dot microdisk lasers," Appl. Phys. Lett. **76**, 3519–3521 (2000).
34. M. Fujita and T. Baba, "Microgear laser," Appl. Phys. Lett. **80**, 2051–2053 (2002).